

Lepton flavor violating decays $l_j \rightarrow l_i \gamma \gamma$

Ming-Yue Liu^{1,2,3}, Shu-Min Zhao^{1,2,3*}, Yi-Tong Wang^{1,2,3}, Xi Wang^{1,2,3}, Xin-Xin Long^{1,2,3},
Tong-Tong Wang^{1,2,3}, Hai-Bin Zhang^{1,2,3}, Tai-Fu Feng^{1,2,3,4}.

¹ *Department of Physics, Hebei University, Baoding 071002, China*

² *Hebei Key Laboratory of High-precision Computation and
Application of Quantum Field Theory, Baoding, 071002, China*

³ *Hebei Research Center of the Basic Discipline for
Computational Physics, Baoding, 071002, China and*

⁴ *Department of Physics, Chongqing University, Chongqing 401331, China*

(Dated: October 31, 2023)

Abstract

In this paper, we study the lepton flavor violating decays of the $l_j \rightarrow l_i \gamma \gamma$ ($j=2, 3$; $i=1, 2$) processes under the $U(1)_X$ SSM. The $U(1)_X$ SSM is the addition of three singlet new Higgs superfields and right-handed neutrinos to the minimal supersymmetric standard model (MSSM). Based on the latest experimental constraints of $l_j \rightarrow l_i \gamma \gamma$, we analyze the effects of different sensitive parameters on the results and made reasonable predictions for future experimental development. Numerical analysis shows that many parameters have a greater or lesser effect on lepton flavor violation(LFV), but the main sensitive parameters and sources leading to LFV are the non-diagonal elements involving the initial and final leptons. This work could provide a basis for the discovery of the existence of new physics (NP).

PACS numbers:

Keywords: lepton flavor violation, $U(1)_X$ SSM, new physics.

* zhaosm@hbu.edu.cn

I. INTRODUCTION

The Standard Model (SM) contains many elementary particles, including fermions and bosons and their various forms. Although the SM has been relatively mature in previous developments, considering the lepton number in the SM, there is not LFV process in the SM [1]. However, the breaking theory of electric weak symmetry and neutrino oscillation experiment show that LFV exists both theoretically and experimentally [2–4], and the experimental observation of charged lepton flavor violation (cLFV) undoubtedly hints at the existence of new physics beyond neutrino oscillations [5]. Any sign of LFV in the experiment could be considered as evidence of LFV existence, and it is necessary to extend the SM through research. Afterwards, scientists extend the SM and obtain many extend models, among which the MSSM has been received much attention, but it is slowly discovered that there are problems in the MSSM such as the μ problem [6] and the zero mass neutrino [7]. To break through these problems we notice the $U(1)$ extension of the MSSM, that is the extension of the MSSM with the $U(1)_X$ gauge group, and the symmetry group is $SU(3)_C \times SU(2)_L \times U(1)_Y \times U(1)_X$ [8–10]. It adds three singlet new Higgs superfields and right-handed neutrino superfields outside the MSSM [11], which relatively perfect solves the problem we face.

The latest upper limits on the LFV branching ratios of $\mu \rightarrow e\gamma\gamma$, $\tau \rightarrow \mu\gamma\gamma$ and $\tau \rightarrow e\gamma\gamma$ at 90% confidence level (CL) [12] are:

$$\begin{aligned} Br(\mu \rightarrow e\gamma\gamma) &< 7.2 \times 10^{-11}, \\ Br(\tau \rightarrow \mu\gamma\gamma) &< 5.8 \times 10^{-4}, \\ Br(\tau \rightarrow e\gamma\gamma) &< 2.5 \times 10^{-4}. \end{aligned} \tag{1}$$

In previous work [13–15], studies have been carried out including a valid field theory analysis to correlate the charged lepton flavor violating processes $l_i \rightarrow l_j\gamma\gamma$ and $l_i \rightarrow l_j\gamma$. Model-independent upper bounds on the $l_i \rightarrow l_j\gamma\gamma$ rates are derived using the current upper bounds on the $l_i \rightarrow l_j\gamma$ rates [13] and in the framework of effective field theory. The magnitude of the branching ratios of $\tau \rightarrow \mu\gamma$ and $\tau \rightarrow \mu\gamma\gamma$ decays caused by a lepton flavor violating Higgs interaction $H\tau\mu$ is studied [14]. Here we will conduct a more comprehensive study of the LFV of the $l_j \rightarrow l_i\gamma\gamma$ under the $U(1)_X$ SSM. We learn about the LFV of the $l_j \rightarrow l_i\gamma$ process [15], and its numerical results show that the experimental limit of the $l_j \rightarrow$

$l_i\gamma$ is the most stringent for the parameter space constraint of the $U(1)_X$ SSM. We study the LFV process of the $l_j \rightarrow l_i\gamma\gamma$ under the $U(1)_X$ SSM in depth on this basis. $l_j \rightarrow l_i\gamma\gamma$ is more complicated and more difficult to study than $l_j \rightarrow l_i\gamma$. Compared with $l_j \rightarrow l_i\gamma$, the Feynman diagrams of $l_j \rightarrow l_i\gamma\gamma$ become more numerous and each of them becomes more complex. We compare the LFVs of the $l_j \rightarrow l_i\gamma$ and $l_j \rightarrow l_i\gamma\gamma$ processes in the numerical section to make our study more interesting and to visualize the correlation between the two type processes. The $l_j \rightarrow l_i\gamma\gamma$ process is a challenging but interesting process. We have derived and numerically analyzed the relevant Feynman diagrams. From the numerical results, we obtain reasonable parameter spaces. The effects of different reasonable parameters on the branching ratio $\text{Br}(l_j \rightarrow l_i\gamma\gamma)$ are compared.

This paper will expand according to the following structure. In Sec.II, we briefly introduce the essential content of the $U(1)_X$ SSM, including its superpotential, the general soft breaking terms, the rotations and interactions of the eigenstates 'EWSB'. In Sec.III, we provide analytical expressions for the branching ratio of the $l_j \rightarrow l_i\gamma\gamma$ decay in the $U(1)_X$ SSM. In Sec.IV, we give the corresponding parameters and numerical analysis. In Sec.V, we present a summary of this article.

II. THE ESSENTIAL CONTENT OF $U(1)_X$ SSM

$U(1)_X$ SSM is a $U(1)$ extension on the basis of MSSM, whose local gauge group is $SU(3)_C \times SU(2)_L \times U(1)_Y \times U(1)_X$ [16–19]. The $U(1)_X$ SSM mainly consists of the superpotential, rotations and interactions for eigenstates 'EWSB' etc. Compared to MSSM, there are new superfields in $U(1)_X$ SSM, such as right-handed neutrinos $\hat{\nu}_i$ and three Higgs singlets $\hat{\eta}$, $\hat{\bar{\eta}}$, \hat{S} . The representation of the superpotential in the $U(1)_X$ SSM is:

$$W = l_W \hat{S} + \mu \hat{H}_u \hat{H}_d + M_S \hat{S} \hat{S} - Y_d \hat{d} \hat{q} \hat{H}_d - Y_e \hat{e} \hat{l} \hat{H}_d + \lambda_H \hat{S} \hat{H}_u \hat{H}_d + \lambda_C \hat{S} \hat{\eta} \hat{\bar{\eta}} + \frac{\kappa}{3} \hat{S} \hat{S} \hat{S} + Y_u \hat{u} \hat{q} \hat{H}_u + Y_X \hat{\nu} \hat{\eta} \hat{\nu} + Y_\nu \hat{\nu} \hat{l} \hat{H}_u. \quad (2)$$

In the above equation, the vacuum expectation values (VEVs) of the two Higgs doublet states H_u, H_d are v_u, v_d and the VEVs of the three Higgs singlet states $\eta, \bar{\eta}, S$ are $v_\eta, v_{\bar{\eta}}$ and v_S respectively. The Higgs superfields are displayed as follows:

$$H_u = \begin{pmatrix} H_u^+ \\ \frac{1}{\sqrt{2}}(v_u + H_u^0 + iP_u^0) \end{pmatrix}, \quad H_d = \begin{pmatrix} \frac{1}{\sqrt{2}}(v_d + H_d^0 + iP_d^0) \\ H_d^- \end{pmatrix},$$

TABLE I: The superfields in $U(1)_X$ SSM

Superfields	\hat{q}_i	\hat{u}_i^c	\hat{d}_i^c	\hat{l}_i	\hat{e}_i^c	$\hat{\nu}_i$	\hat{H}_u	\hat{H}_d	$\hat{\eta}$	$\hat{\bar{\eta}}$	\hat{S}
$SU(3)_C$	3	$\bar{3}$	$\bar{3}$	1	1	1	1	1	1	1	1
$SU(2)_L$	2	1	1	2	1	1	2	2	1	1	1
$U(1)_Y$	1/6	-2/3	1/3	-1/2	1	0	1/2	-1/2	0	0	0
$U(1)_X$	0	-1/2	1/2	0	1/2	-1/2	1/2	-1/2	-1	1	0

$$\eta = \frac{1}{\sqrt{2}}(v_\eta + \phi_\eta^0 + iP_\eta^0), \quad \bar{\eta} = \frac{1}{\sqrt{2}}(v_{\bar{\eta}} + \phi_{\bar{\eta}}^0 + iP_{\bar{\eta}}^0), \quad S = \frac{1}{\sqrt{2}}(v_S + \phi_S^0 + iP_S^0). \quad (3)$$

There are two angles $\tan \beta$ and $\tan \beta_\eta$, which are defined as $\tan \beta = v_u/v_d$ and $\tan \beta_\eta = v_{\bar{\eta}}/v_\eta$.

The soft SUSY breaking terms of $U(1)_X$ SSM are shown as:

$$\begin{aligned} \mathcal{L}_{soft} = & \mathcal{L}_{soft}^{MSSM} - B_S S^2 - L_S S - \frac{T_\kappa}{3} S^3 - T_{\lambda_C} S \eta \bar{\eta} + \epsilon_{ij} T_{\lambda_H} S H_d^i H_u^j \\ & - T_X^{IJ} \bar{\eta} \tilde{\nu}_R^{*I} \tilde{\nu}_R^{*J} + \epsilon_{ij} T_\nu^{IJ} H_u^i \tilde{\nu}_R^{I*} \tilde{l}_j^J - m_\eta^2 |\eta|^2 - m_{\bar{\eta}}^2 |\bar{\eta}|^2 - m_S^2 S^2 \\ & - (m_{\tilde{\nu}_R}^2)^{IJ} \tilde{\nu}_R^{I*} \tilde{\nu}_R^J - \frac{1}{2} \left(M_S \lambda_{\tilde{X}}^2 + 2 M_{BB'} \lambda_{\tilde{B}} \lambda_{\tilde{X}} \right) + h.c. \end{aligned} \quad (4)$$

The particle content and charge assignments for $U(1)_X$ SSM are shown in the Table I. The new effect of the gauge kinetic mixing in $U(1)_X$ SSM has never been seen before in MSSM. Here $U(1)_Y$ and $U(1)_X$ are two Abelian groups, and we denote $U(1)_Y$ charge by Y^Y and $U(1)_X$ charge by Y^X . They generate the gauge kinetic mixing. The rotations of eigenstates 'EWSB' are divided into two categories. One is rotation in mass sector and the other is rotation in gauge sector. Rotations in gauge sector for eigenstates 'EWSB' are:

$$\begin{aligned} \begin{pmatrix} B_\rho \\ W_{3\rho} \\ V_{B_X} \end{pmatrix} &= Z^{\gamma Z Z'} \begin{pmatrix} \gamma_\rho \\ Z_\rho \\ Z'_\rho \end{pmatrix}, \quad \begin{pmatrix} \lambda_{\tilde{W},1} \\ \lambda_{\tilde{W},2} \\ \lambda_{\tilde{W},3} \end{pmatrix} = Z^{\tilde{W}} \begin{pmatrix} \tilde{W}^- \\ \tilde{W}^+ \\ \tilde{W}^0 \end{pmatrix}, \\ &\begin{pmatrix} W_{1\rho} \\ W_{2\rho} \end{pmatrix} = Z^W \begin{pmatrix} W_\rho^- \\ W_\rho^- \end{pmatrix}. \end{aligned} \quad (5)$$

θ_W is the Weinberg angle, the mixing matrices are parametrized by:

$$Z^{\gamma Z Z'} = \begin{pmatrix} \cos \theta_W & -\cos \theta'_W \sin \theta_W & \sin \theta_W \sin \theta'_W \\ \sin \theta_W & \cos \theta_W \sin \theta'_W & -\cos \theta_W \sin \theta'_W \\ 0 & \sin \theta'_W & \cos \theta'_W \end{pmatrix},$$

$$Z^W = \begin{pmatrix} \frac{1}{\sqrt{2}} & \frac{1}{\sqrt{2}} \\ -i\frac{1}{\sqrt{2}} & i\frac{1}{\sqrt{2}} \end{pmatrix}, \quad Z^{\tilde{W}} = \begin{pmatrix} \frac{1}{\sqrt{2}} & \frac{1}{\sqrt{2}} & 0 \\ -i\frac{1}{\sqrt{2}} & i\frac{1}{\sqrt{2}} & 0 \\ 0 & 0 & 1 \end{pmatrix}. \quad (6)$$

There are mass matrices for scalars and fermions. The mass squared matrix for CP -odd sneutrino (σ_l, σ_r) reads:

$$M_{\nu^I}^2 = \begin{pmatrix} m_{\sigma_l \sigma_l} & m_{\sigma_r \sigma_l}^T \\ m_{\sigma_l \sigma_r} & m_{\sigma_r \sigma_r} \end{pmatrix}, \quad (7)$$

$$m_{\sigma_l \sigma_l} = \frac{1}{8} \left((g_1^2 + g_{YX}^2 + g_2^2 + g_{YX} g_X)(v_d^2 - v_u^2) + 2g_{YX} g_X (v_\eta^2 - v_{\bar{\eta}}^2) \right) + \frac{1}{2} v_u^2 Y_\nu^T Y_\nu + M_L^2, \quad (8)$$

$$m_{\sigma_l \sigma_r} = \frac{1}{\sqrt{2}} v_u T_\nu - v_u v_{\bar{\eta}} Y_X Y_\nu - \frac{1}{2} v_d (\lambda_H v_S + \sqrt{2} \mu) Y_\nu, \quad (9)$$

$$m_{\sigma_r \sigma_r} = \frac{1}{8} \left((g_{YX} g_X + g_X^2)(v_d^2 - v_u^2) + 2g_X^2 (v_\eta^2 - v_{\bar{\eta}}^2) \right) - v_\eta v_S Y_X \lambda_C + M_\nu^2 + \frac{1}{2} v_u^2 |Y_\nu|^2 + v_{\bar{\eta}} (2v_{\bar{\eta}} Y_X Y_X - \sqrt{2} T_X). \quad (10)$$

The mass squared matrix for CP -even sneutrino (ϕ_l, ϕ_r) reads:

$$M_{\nu^R}^2 = \begin{pmatrix} m_{\phi_l \phi_l} & m_{\phi_r \phi_l}^T \\ m_{\phi_l \phi_r} & m_{\phi_r \phi_r} \end{pmatrix}, \quad (11)$$

$$m_{\phi_l \phi_l} = \frac{1}{8} \left((g_1^2 + g_{YX}^2 + g_2^2 + g_{YX} g_X)(v_d^2 - v_u^2) + g_{YX} g_X (2v_\eta^2 - 2v_{\bar{\eta}}^2) \right) + \frac{1}{2} v_u^2 Y_\nu^T Y_\nu + M_L^2, \quad (12)$$

$$m_{\phi_l \phi_r} = \frac{1}{\sqrt{2}} v_u T_\nu + v_u v_{\bar{\eta}} Y_X Y_\nu - \frac{1}{2} v_d (\lambda_H v_S + \sqrt{2} \mu) Y_\nu, \quad (13)$$

$$m_{\phi_r \phi_r} = \frac{1}{8} \left((g_{YX} g_X + g_X^2)(v_d^2 - v_u^2) + 2g_X^2 (v_\eta^2 - v_{\bar{\eta}}^2) \right) + v_\eta v_S Y_X \lambda_C + M_\nu^2 + \frac{1}{2} v_u^2 |Y_\nu|^2 + v_{\bar{\eta}} (2v_{\bar{\eta}} Y_X Y_X + \sqrt{2} T_X). \quad (14)$$

The mass matrix for chargino reads:

$$m_{\tilde{\chi}^-} = \begin{pmatrix} M_2 & \frac{1}{\sqrt{2}} g_2 v_\mu \\ \frac{1}{\sqrt{2}} g_2 v_d & \frac{1}{\sqrt{2}} \lambda_H v_S + \mu \end{pmatrix}. \quad (15)$$

This matrix is diagonalized by U and V:

$$U^* m_{\tilde{\chi}^-} V^\dagger = m_{\tilde{\chi}^-}^{diag}, \quad (16)$$

with

$$\begin{aligned} \tilde{W}^- &= \sum_{t_2} U_{j1}^* \lambda_j^-, & \tilde{H}_d^- &= \sum_{t_2} U_{j2}^* \lambda_j^-, \\ \tilde{W}^+ &= \sum_{t_2} V_{1j}^* \lambda_j^+, & \tilde{H}_u^- &= \sum_{t_2} V_{2j}^* \lambda_j^+. \end{aligned} \quad (17)$$

Furthermore, some other required mass matrices can be found in Refs.[16, 17]. There are interactions between the eigenstates 'EWSB', and here we list some of the couplings required in the $U(1)_X$ SSM. We derive the vertices of lepton-chargino-sneutrino:

$$\begin{aligned} \mathcal{L}_{\tilde{l}_X^- \tilde{\nu}^I} &= \frac{i}{\sqrt{2}} \bar{l}_i \left\{ U_{j2}^* Z_{ki}^{I*} Y_l^i P_L - g_2 V_{j1} Z_{ki}^{I*} P_R \right\} \chi_j^- \tilde{\nu}_k^I, \\ \mathcal{L}_{\tilde{l}_X^- \tilde{\nu}^R} &= \frac{1}{\sqrt{2}} \bar{l}_i \left\{ U_{j2}^* Z_{ki}^{R*} Y_l^i P_L - g_2 V_{j1} Z_{ki}^{R*} P_R \right\} \chi_j^- \tilde{\nu}_k^R. \end{aligned} \quad (18)$$

We also derive the vertex of neutralino-lepton-slepton:

$$\begin{aligned} \mathcal{L}_{\tilde{\chi}^0 l \tilde{L}} &= \bar{\chi}_i^0 \left\{ \left(\frac{1}{\sqrt{2}} (g_1 N_{i1}^* + g_2 N_{i2}^* + g_{YX} N_{i5}^*) Z_{kj}^E - N_{i3}^* Y_l^j Z_{K(3+j)}^E \right) P_L, \right. \\ &\quad \left. - \left[\frac{1}{\sqrt{2}} (2g_1 N_{i1} + (2g_{YX} + g_X) N_{i5}) Z_{k(3+a)}^E + Y_l^j Z_{kj}^E N_{i3} \right] P_R \right\} l_j \tilde{L}_k. \end{aligned} \quad (19)$$

There are some other vertices being needed, and to save space in this text, the remaining vertices can be found in Refs.[18–21].

III. FORMULATION

In this section, we study the amplitude and branching ratio of $l_j \rightarrow l_i \gamma \gamma$ ($j = 2, 3; i = 1, 2$). Here, we do not extract the operators as in the previous work [12, 15], but do a more comprehensive process. The corresponding Feynman diagrams are shown in Fig.1. We study two-photon with q_1 and q_2 representing the momentums of the two photons, respectively. In Fig.1 all diagrams except Fig.1(c) contain diagrams with q_1 on the left and q_2 on the right and with the positions of q_1 and q_2 switched.

We choose a Feynman diagram in Fig.1 to analyze. The Feynman amplitude of Fig.1(a) is:

$$\mathcal{M}_{(a)} = \bar{U}_i(p + q_1 + q_2) \int \frac{d^D k}{(2\pi)^D} \frac{1}{[(k + p + q_1 + q_2)^2 - m_f^2][(k + p + q_1)^2 - m_f^2][(p + k)^2 - m_f^2]}$$

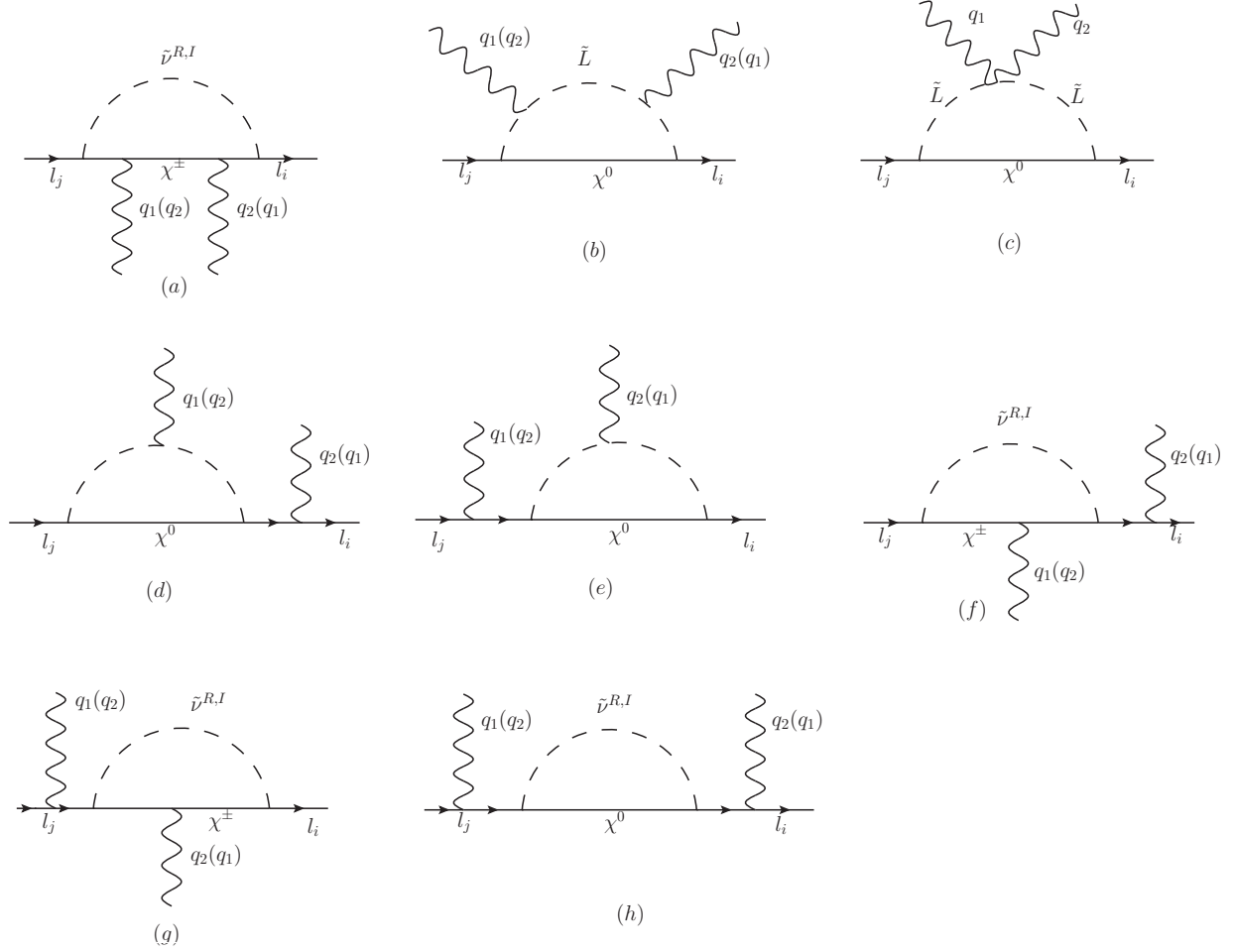


FIG. 1: Feynman diagrams for the $l_j \rightarrow l_i \gamma \gamma$ processes in the $U(1)_X$ SSM.

$$\frac{1}{(k^2 - m_s^2)} \left((A_L P_L + A_R P_R) (\not{k} + \not{p} + \not{q}_1 + \not{q}_2 + m_f) \gamma^\nu e (\not{k} + \not{p} + \not{q}_1 + m_f) \gamma^\mu e \right. \\ \left. (\not{k} + \not{p} + m_f) (B_L P_L + B_R P_R) \right) U_j(p) \varepsilon_\mu^*(q_1) \varepsilon_\nu^*(q_2), \quad (20)$$

where p is the injected lepton momentum, m_f corresponds to the chargino mass, m_s corresponds to the scalar neutrino (CP -even or CP -odd) mass. A_L, B_L, A_R and B_R represent the coupling vertices we mentioned in Sec.II. $\mathcal{L} = \bar{F}_1(iA_L + iA_R)F_2S$, $\bar{U}_i(p + q_1 + q_2)$ and $U_j(p)$ are the wave functions of the external leptons.

Since the mass of the inner particle is large and the mass of the outer particle is small. So, for the denominator term in $\mathcal{M}_{(a)}$ we can do the following expansion to simplify the calculation

$$\frac{1}{(k + p)^2 - m_f^2} = \frac{1}{k^2 - m_f^2} \left(1 - \frac{p^2 + 2k \cdot p}{k^2 - m_f^2} + \frac{4(k \cdot p)^2}{(k^2 - m_f^2)^2} \right). \quad (21)$$

We take all the diagrams in Fig.1 as above and further simplify them. Since the results produced by its computational process are very large, we use *Mathematica* \ll *HighEnergyPhysics'FeynCalc'* for analytical calculations. We derive the Feynman amplitudes of all the diagrams, using the on-shell condition, so that $q_1^2 = 0$, $q_2^2 = 0$, $p^2 = m_f^2$. Summation is performed and its mode square is calculated as $|\mathcal{M}|^2$. In $|\mathcal{M}|^2$ there are various loop functions such as $A_L B_R \frac{k^2}{(k^2 - m_s^2)^3 (k^2 - m_f^2)} m_f^2$, $A_R B_L \frac{k^4}{(k^2 - m_s^2)^4 (k^2 - m_f^2)} m_f^3$, $A_R B_L \frac{1}{(k^2 - m_s^2)(k^2 - m_f^2)^3} m_f^2$ and so on, make $x = \frac{m_s^2}{m_\omega^2}$, $y = \frac{m_f^2}{m_\omega^2}$.

Here:

$$\begin{aligned} \int \frac{d^D k}{(2\pi)^D} \frac{k^2}{(k^2 - m_s^2)^3 (k^2 - m_f^2)} &= \frac{i}{32\pi^2} \left(\frac{2y^2(\log(x) + \log(y))}{(y-x)^3} + \frac{3y-x}{(x-y)^2} \right), \\ \int \frac{d^D k}{(2\pi)^D} \frac{k^4}{(k^2 - m_s^2)^4 (k^2 - m_f^2)} &= \frac{i}{96\pi^2} \left(\frac{7xy - 2x^2 - 11y^2}{(x-y)^3} + \frac{6y^3(\log(x) - \log(y))}{(x-y)^4} \right), \\ \int \frac{d^D k}{(2\pi)^D} \frac{1}{(k^2 - m_s^2)(k^2 - m_f^2)^3} &= \frac{i}{32\pi^2} \left(\frac{x+y}{y(x-y)^2} - \frac{2x(\log(x) - \log(y))}{(x-y)^3} \right). \end{aligned} \quad (22)$$

In order to obtain the branching ratio, we derive the three-body decay (Fig.2) by defining $p_i + q_j = p_{ij}$, $p_{ij}^2 = m_{ij}^2$. With total energy E , the momentums of the three final state particles are in the same plane and their relative directions are fixed. Let their Euler angles be (α, β, γ) to determine the final system with respect to the initial orientation of the particles, we obtain:

$$d\Gamma = \frac{1}{(2\pi)^5} \frac{1}{16M} |\mathcal{M}|^2 dE_1 dE_3 d\alpha d(\cos \beta) d\gamma. \quad (23)$$

If the decaying particle is a scalar or we average over its spin state, then the integration in terms of the equation is:

$$d\Gamma = \frac{1}{(2\pi)^3} \frac{1}{8M} |\mathcal{M}|^2 dE_1 dE_3. \quad (24)$$

We integrate the E_1 , E_2 in $|\mathcal{M}|^2$, $0 \leq E_1 \leq \frac{m_j}{2}$, $\frac{m_j}{2} - E_1 \leq E_2 \leq \frac{m_j}{2}$. We obtain the decay width and branching ratio as:

$$\Gamma(l_j \rightarrow l_i \gamma \gamma) = \frac{1}{(2\pi)^3} \frac{1}{8M} \int |\mathcal{M}|^2 dE_1 dE_2, \quad (25)$$

$$Br(l_j \rightarrow l_i \gamma \gamma) = \frac{\Gamma(l_j \rightarrow l_i \gamma \gamma)}{\Gamma_{l_j}}. \quad (26)$$

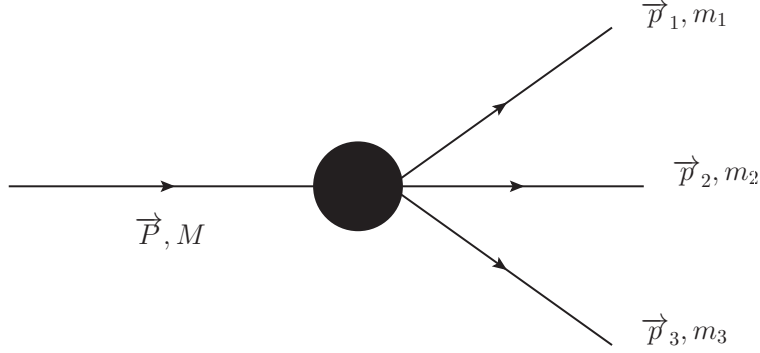


FIG. 2: Definitions of variables for three-body decays.

IV. NUMERICAL ANALYSIS

In this section, we perform numerical results considering experimental constraints on the lepton flavor violating process $l_j \rightarrow l_i \gamma \gamma$ and the lightest CP -even Higgs mass $m_{h0} = 125.25$ GeV [12, 22, 23]. We need to find some sensitive parameters from the parameters used, so as to obtain reasonable numerical results. Since the experimental limit of the $l_j \rightarrow l_i \gamma$ [15] process has the most stringent parameter space constraint on the $U(1)_X$ SSM, we need to consider the effect of $l_j \rightarrow l_i \gamma$ on the LFV. The strongest limit of $\mu \rightarrow e \gamma$, and the other limits can be satisfied if the limit of $\mu \rightarrow e \gamma$ is satisfied [16]. So we plot $l_j \rightarrow l_i \gamma$ processes with the same parameters as the $l_j \rightarrow l_i \gamma \gamma$ processes, so that we can ensure that the studied processes strictly satisfy the $l_j \rightarrow l_i \gamma$ constraints. According to the latest data from the LHC, we take for the scalar lepton mass greater than 700 GeV, the chargino mass greater than 1100 GeV, for more detailed limits refer to Refs.[24–29]. We will discuss the processes $\mu \rightarrow e \gamma \gamma$, $\tau \rightarrow \mu \gamma \gamma$, $\tau \rightarrow e \gamma \gamma$ in three subsections and plot the relational and scatter diagrams with different parameters. By analyzing these plots and the experimental limits of the branching ratios, a reasonable parameter space is found to explain the LFV.

In summary, considering the experimental constraints described above, we adopt the following parameters in the numerical calculation.

$$\begin{aligned}
 \mu &= M_{BL} = T_{\lambda_C} = T_{\lambda_H} = T_{\kappa} = 1 \text{ TeV}, \quad M_{BB'} = M_S = 0.4 \text{ TeV}, \quad \lambda_H = 0.1, \\
 l_W &= B_{\mu} = B_S = 0.1 \text{ TeV}^2, \quad T_{Xii} = -1 \text{ TeV}, \quad \kappa = 0.1, \quad Y_{Xii} = 1 \text{ TeV} (i = 1, 2, 3), \\
 M_{Eii}^2 &= 0.8 \text{ TeV}^2, \quad M_{\nu ii}^2 = 0.3 \text{ TeV}^2, \quad T_{\tilde{e}ii} = 0.5 \text{ TeV}, \quad \lambda_C = -0.25.
 \end{aligned} \tag{27}$$

To simplify the numerical study, we use the relation of the parameters, which vary in the

numerical analysis below

$$\begin{aligned}
M_{\tilde{L}ij}^2 &= M_{\tilde{L}ji}^2, \quad T_{eij} = T_{eji}, \quad M_{\tilde{E}ii}^2 = M_{\tilde{E}}^2, \quad M_{\tilde{L}ii}^2 = M_{\tilde{L}}^2, \quad M_{\tilde{\nu}ij}^2 = M_{\tilde{\nu}ji}^2, \\
M_{\tilde{E}ij}^2 &= M_{\tilde{E}ji}^2, \quad g_{YX}, \quad M_2, \quad \tan \beta, \quad g_X, \quad (i, j = 1, 2, 3, i \neq j).
\end{aligned} \tag{28}$$

Normally, the non-diagonal elements of the parameters are defined to be zero, unless we specify otherwise.

A. $\mu \rightarrow e\gamma\gamma$

We perform numerical calculation for $\text{Br}(\mu \rightarrow e\gamma\gamma)$ and plot the relationship and scatter diagrams for different parameters in order to clearly show the numerical results. In Fig.3 the gray area is the experimental limit satisfied by the processes.

With the parameters $M_{\tilde{L}}^2 = 1 \times 10^6 \text{ GeV}^2$, $g_X = 0.3$, we plot $\text{Br}(\mu \rightarrow e\gamma\gamma)$ and $\text{Br}(\mu \rightarrow e\gamma)$ versus M_2 in the Fig.3(a)(e). The dashed lines correspond to $\tan \beta = 25$ and the solid lines correspond to $\tan \beta = 20$. We find that lines decrease with increasing M_2 in the range of 700 GeV-2500 GeV. The dashed lines are larger than the solid lines, and both the solid and dashed lines are located in the gray area indicating that both are within the experimental limits. In the Fig.3(b), we plot $\text{Br}(\mu \rightarrow e\gamma\gamma)$ versus $M_{\tilde{L}12}^2$, in which the dashed line corresponds to $M_2 = 1600 \text{ GeV}$ and the solid line corresponds to $M_2 = 1200 \text{ GeV}$. We find that two lines increase with increasing $M_{\tilde{L}12}^2$ in the range of $0 - 5 \times 10^4 \text{ GeV}^2$. The solid line is larger than the dashed line, and both the solid and dashed lines are located in the gray area satisfying the experimental limits.

In the Fig.3(c), we plot $\text{Br}(\mu \rightarrow e\gamma\gamma)$ versus $M_{\tilde{E}}^2$, in which the dashed line corresponds to $T_{e13} = 200 \text{ GeV}$ and the solid line corresponds to $T_{e13} = 100 \text{ GeV}$. We find that two lines decrease with increasing $M_{\tilde{E}}^2$ in the range of $0 - 4 \times 10^5 \text{ GeV}^2$. The dashed line is larger than the solid line. Both the solid and dashed lines are located in the gray area indicating that both are within the experimental limits. In Fig.3(d)(f) we let $\tan \beta = 20$, $M_2 = 1200 \text{ GeV}$, $M_{\tilde{E}}^2 = 8 \times 10^5 \text{ GeV}^2$, and plot $\text{Br}(\mu \rightarrow e\gamma\gamma)$ and $\text{Br}(\mu \rightarrow e\gamma)$ versus $M_{\tilde{E}12}^2$, with $g_{YX} = 0.1$ (dashed line), $g_{YX} = 0.2$ (solid line). It is clear that, both lines increase gradually, meaning that $\text{Br}(\mu \rightarrow e\gamma\gamma)$ and $\text{Br}(\mu \rightarrow e\gamma)$ get larger as $M_{\tilde{E}12}^2$ increase. As solid and dashed lines go from bottom to top, $\text{Br}(\mu \rightarrow e\gamma\gamma)$ and $\text{Br}(\mu \rightarrow e\gamma)$ increases as g_{YX} decreases.

$M_{\tilde{L}12}^2$ and $M_{\tilde{E}}^2$ are flavor parameters that appear in the slepton, CP -even sneutrino and

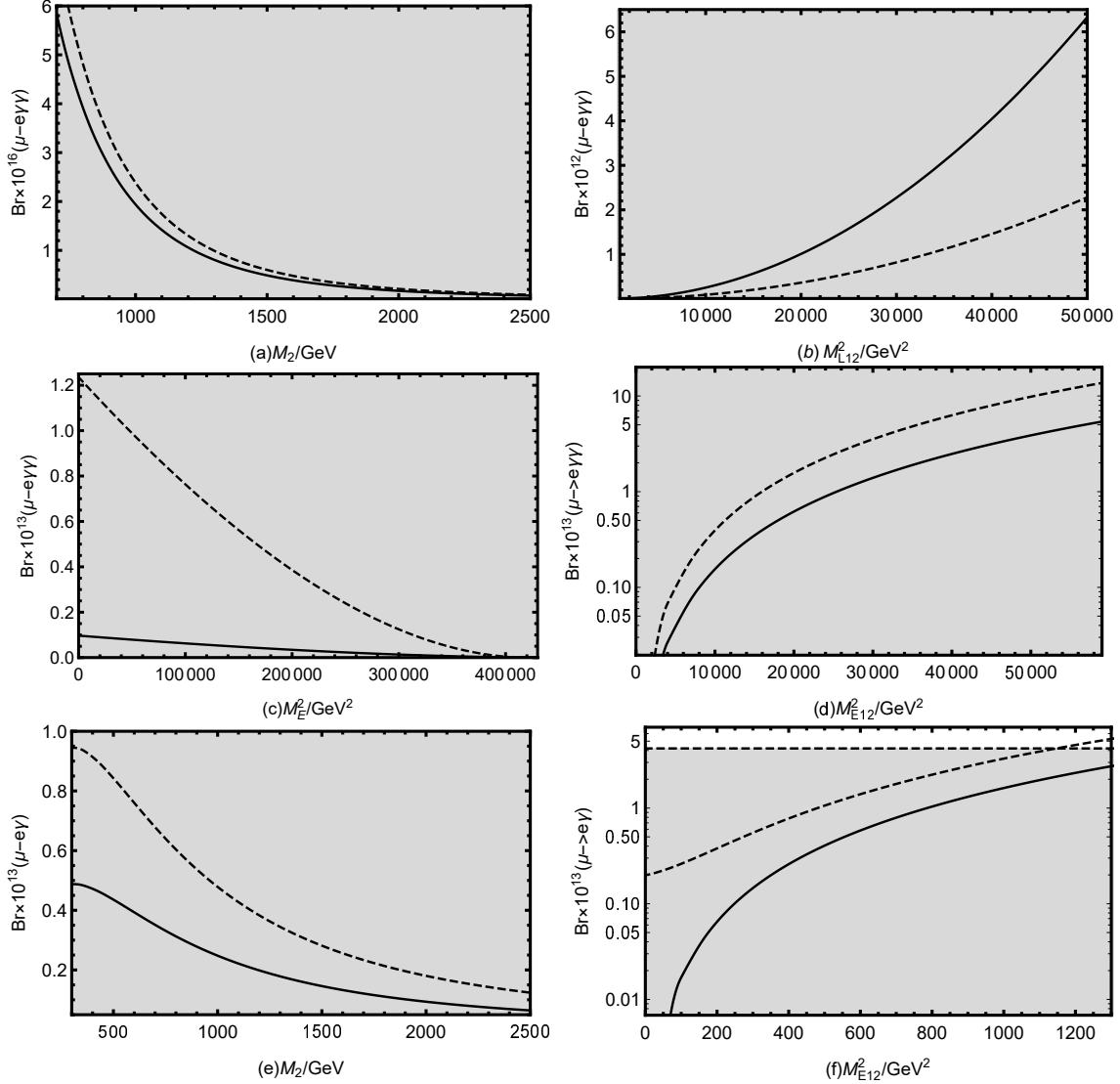


FIG. 3: $\text{Br}(\mu \rightarrow e\gamma\gamma)$ and $\text{Br}(\mu \rightarrow e\gamma)$ schematic diagrams affected by different parameters. The gray areas are reasonable value range, where $\text{Br}(\mu \rightarrow e\gamma\gamma)$ and $\text{Br}(\mu \rightarrow e\gamma)$ are lower than the upper limit. The dashed and solid lines in Fig.3(a)(e) correspond to $\tan\beta = 25$ and $\tan\beta = 20$. The dashed and solid lines in Fig.3(b) correspond to $M_2 = 1600$ GeV and $M_2 = 1200$ GeV. The dashed and solid lines in Fig.3(c) correspond to $T_{e13} = 200$ GeV and $T_{e13} = 100$ GeV. In Fig.3(d)(f), the $g_{YX} = 0.1$ (dashed line) and $g_{YX} = 0.2$ (solid line).

CP -odd sneutrino mass matrices. $\text{Br}(\mu \rightarrow e\gamma\gamma)$ decreases with increasing parameters M_2 and M_E^2 and increases with increasing M_{L12}^2 . In Fig.3(a)(c), the slopes of the dashed lines are higher than the solid lines, meaning that the larger $\tan\beta$ and T_{e13} , the greater the slopes. While in Fig.3(b), the larger M_2 , the smaller the slope. In Fig.3, M_2 , M_{L12}^2 and M_E^2 vary

TABLE II: Scanning parameters for Fig.4, Fig.6 and Fig.8.

Parameters	$\tan \beta$	g_X	g_{YX}	λ_H	λ_C	μ/GeV	M_2/GeV	M_L^2/GeV^2	M_ν^2/GeV^2
Min	5	0.3	0.01	0.1	-0.3	1000	700	4×10^5	3×10^5
Max	50	0.6	0.2	0.3	-0.1	1300	2500	5×10^6	5×10^6

much less than their current limits in the $10^{-16} - 10^{-12}$ region. In summary, M_2 , $M_{\tilde{L}12}^2$, $M_{\tilde{E}12}^2$ and $M_{\tilde{E}}^2$ are sensitive parameters that have a significant effect on $\text{Br}(\mu \rightarrow e\gamma\gamma)$.

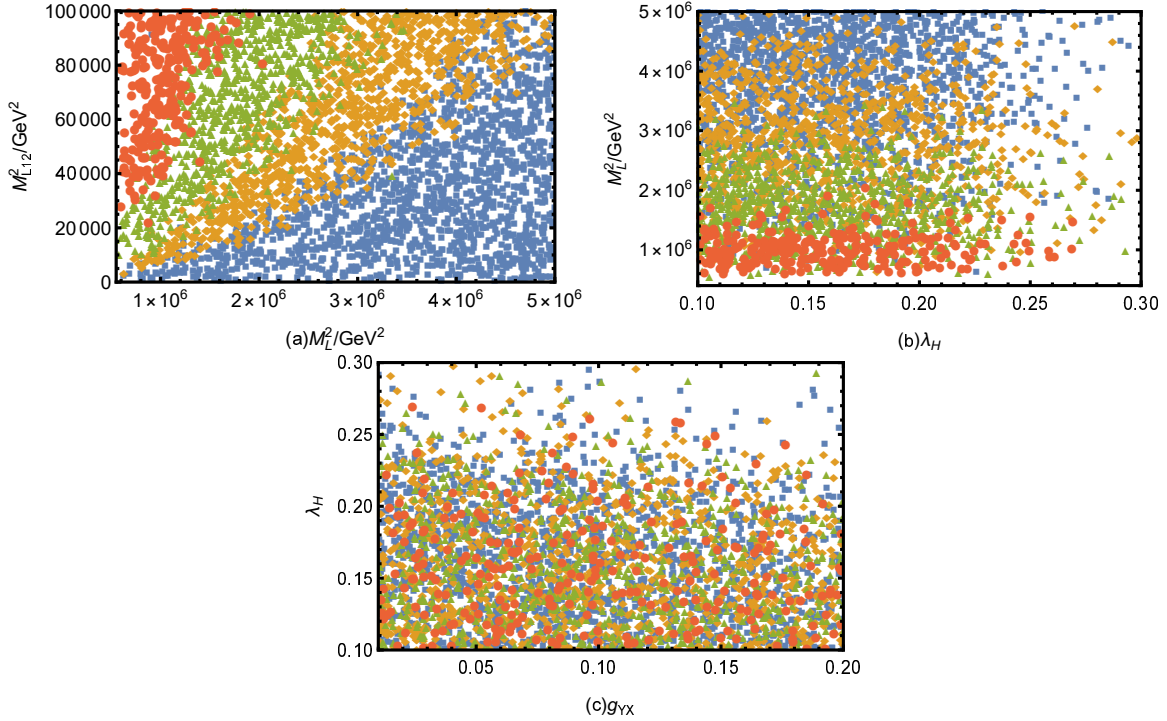


FIG. 4: Under the premise of current limit on LFV decay $\mu \rightarrow e\gamma\gamma$, reasonable parameter space is selected to scatter points, with the notation \blacksquare ($0 < \text{Br}(\mu \rightarrow e\gamma\gamma) < 6 \times 10^{-14}$), \blacklozenge ($6 \times 10^{-14} \leq \text{Br}(\mu \rightarrow e\gamma\gamma) < 3 \times 10^{-13}$), \blacktriangle ($3 \times 10^{-13} \leq \text{Br}(\mu \rightarrow e\gamma\gamma) < 3 \times 10^{-12}$), \bullet ($3 \times 10^{-12} \leq \text{Br}(\mu \rightarrow e\gamma\gamma) < 7.2 \times 10^{-11}$).

Next, we randomly scan some parameters, which we represent in a tabular form. Fig.4 is obtained from the parameters shown in Table II and Table III. We use \blacksquare ($0 < \text{Br}(\mu \rightarrow e\gamma\gamma) < 6 \times 10^{-14}$), \blacklozenge ($6 \times 10^{-14} \leq \text{Br}(\mu \rightarrow e\gamma\gamma) < 3 \times 10^{-13}$), \blacktriangle ($3 \times 10^{-13} \leq \text{Br}(\mu \rightarrow e\gamma\gamma) < 3 \times 10^{-12}$), \bullet ($3 \times 10^{-12} \leq \text{Br}(\mu \rightarrow e\gamma\gamma) < 7.2 \times 10^{-11}$) to represent the results for different parameter spaces for the $\mu \rightarrow e\gamma\gamma$ process respectively.

Analysis of the relationship between $M_{\tilde{L}12}^2$ and M_L^2 is shown in Fig.4(a). The overall

TABLE III: Scanning parameters for Fig.4.

Parameters	M_{L12}^2 / GeV^2	T_{e12} / GeV	$T_{\bar{\nu}12} / \text{GeV}$
Min	0	- 400	- 400
Max	10^5	400	400

trend is obvious. With \bullet mainly concentrated in the upper left corner, the outer layer is \blacktriangle , followed by \blacklozenge , and the rightmost is \blacksquare . When M_{L12}^2 approaches $1 \times 10^5 \text{ GeV}^2$ and M_L^2 approaches $4 \times 10^5 \text{ GeV}^2$, $\text{Br}(\mu \rightarrow e\gamma\gamma)$ gets the maximum value. In Fig.4(b) we analyze the relationship between M_L^2 and λ_H , and we find that the trend of dispersion is weak, where \bullet part is mainly in $4 \times 10^5 < M_L^2 \leq 1.4 \times 10^6$, \blacktriangle is mainly in $1.4 \times 10^6 < M_L^2 \leq 2.4 \times 10^6$, \blacklozenge is mainly in $2.4 \times 10^6 < M_L^2 \leq 4.2 \times 10^6$, \blacksquare is mainly in $4.2 \times 10^6 < M_L^2 \leq 5 \times 10^6$. The four color levels are obvious, and the value of $\text{Br}(\mu \rightarrow e\gamma\gamma)$ increases as M_L^2 decreases. Fig.4(c) shows the effects of λ_H and g_{YX} on $\text{Br}(\mu \rightarrow e\gamma\gamma)$. All points are mainly concentrated near the x-axis. We find that it is denser in the range of $0.1 < \lambda_H \leq 0.2$ and increasingly sparse in the range of $0.2 < \lambda_H \leq 0.3$.

B. $\tau \rightarrow \mu\gamma\gamma$

With the parameters $M_E^2 = 8 \times 10^5 \text{ GeV}^2$, $M_L^2 = 1 \times 10^6 \text{ GeV}^2$, $M_2 = 1200 \text{ GeV}$, $\tan\beta = 20$, $g_X=0.3$, we plot the schematic diagram of $\text{Br}(\tau \rightarrow \mu\gamma\gamma)$ affected by different parameters. The relationship between $\text{Br}(\tau \rightarrow \mu\gamma\gamma)$ and the parameter M_{E23}^2 is plotted in Fig.5(d) utilizing the same parameters as in Fig.5(b).

We study the effects of parameters g_{YX} , M_{E23}^2 and T_{e23} on $\text{Br}(\tau \rightarrow \mu\gamma\gamma)$ in Fig.5. In Fig.5(a) we set $M_{\bar{\nu}12}^2 = 100 \text{ GeV}^2$ and plot the relationship between $\text{Br}(\tau \rightarrow \mu\gamma\gamma)$ and g_{YX} , where the dashed line corresponds to $M_{E23}^2 = 2000 \text{ GeV}^2$ and the solid line corresponds to $M_{E23}^2 = 1000 \text{ GeV}^2$. The dashed line is larger than the solid line. We can clearly see that these two lines decrease as g_{YX} increases. The solid and dashed lines are located in the gray area. In Fig.5(b)(d), the relationship between $\text{Br}(\tau \rightarrow \mu\gamma\gamma)$, $\text{Br}(\tau \rightarrow \mu\gamma)$ and M_{E23}^2 are shown, and the results are plotted with the dashed lines ($M_{L23}^2 = 2000 \text{ GeV}^2$) and the solid lines ($M_{L23}^2 = 200 \text{ GeV}^2$), respectively. We find that lines show an increasing trend, and their values gradually coincide as M_{E23}^2 increases. Both are smaller than the experimental upper limit.

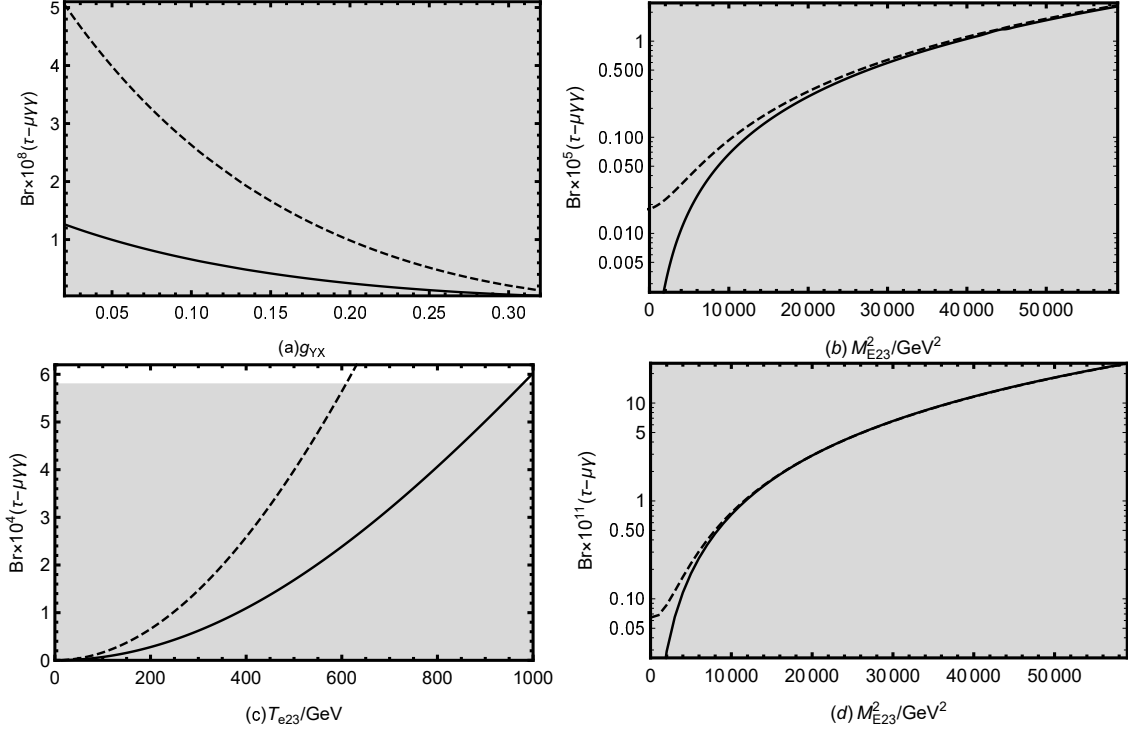


FIG. 5: $\text{Br}(\tau \rightarrow \mu\gamma\gamma)$ and $\text{Br}(\tau \rightarrow \mu\gamma)$ diagrams affected by different parameters. The gray areas are reasonable value range. With $M_{\nu 12}^2 = 100 \text{ GeV}^2$, the dashed and solid lines in Fig.5(a) correspond to $M_{E23}^2 = 2000 \text{ GeV}^2$ and $M_{E23}^2 = 1000 \text{ GeV}^2$. The dashed and solid lines in Fig.5(b)(d) correspond to $M_{L23}^2 = 2000 \text{ GeV}^2$ and $M_{L23}^2 = 200 \text{ GeV}^2$. As $M_{L23}^2 = 500 \text{ GeV}^2$, the dashed and solid lines in Fig.5(c) correspond to $M_2 = 1600 \text{ GeV}$ and $M_2 = 1200 \text{ GeV}$.

TABLE IV: Scanning parameters for Fig.6

Parameters	M_{L23}^2 / GeV^2	T_{e23} / GeV	$T_{\nu 23} / \text{GeV}$
Min	0	- 400	- 400
Max	10^5	400	400

In Fig.5(c), $\text{Br}(\tau \rightarrow \mu\gamma\gamma)$ varies with T_{e23} as $M_{L23}^2 = 500 \text{ GeV}^2$, the dashed and solid lines correspond to $M_2 = 1600 \text{ GeV}$ and $M_2 = 1200 \text{ GeV}$, respectively. It can be clearly seen that both the solid and dashed lines have a tendency to rise. The rising range of the dashed line is larger than that of the solid line. The dashed line with T_{e23} range of 0 – 600 GeV and the solid line with T_{e23} range of 0 – 960 GeV lie within the experimental limits. In summary the parameters g_{YX} , M_{E23}^2 and T_{e23} have influence on $\text{Br}(\tau \rightarrow \mu\gamma\gamma)$ and are sensitive parameters.

Next, we randomly scan some parameters, namely those shown in Table II and Table

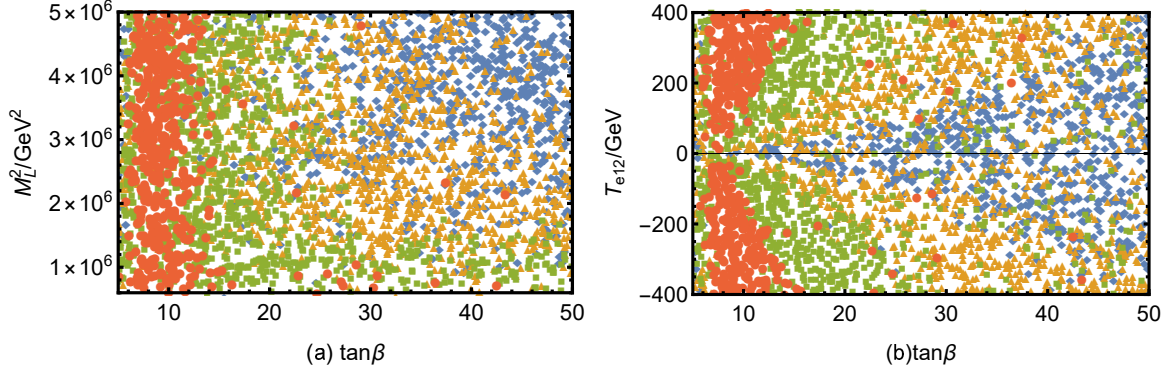


FIG. 6: Under the premise of current limit on LFV decay $\tau \rightarrow \mu\gamma\gamma$, reasonable parameter space is selected to scatter points, with the notation \blacklozenge ($0 < Br(\tau \rightarrow \mu\gamma\gamma) < 4 \times 10^{-6}$), \blacktriangle ($4 \times 10^{-6} \leq Br(\tau \rightarrow \mu\gamma\gamma) < 4 \times 10^{-5}$), \blacksquare ($4 \times 10^{-5} \leq Br(\tau \rightarrow \mu\gamma\gamma) < 5.8 \times 10^{-4}$), \bullet ($Br(\tau \rightarrow \mu\gamma\gamma) \geq 5.8 \times 10^{-4}$).

IV, according to which we obtain Fig.6. We use \blacklozenge ($0 < Br(\tau \rightarrow \mu\gamma\gamma) < 4 \times 10^{-6}$), \blacktriangle ($4 \times 10^{-6} \leq Br(\tau \rightarrow \mu\gamma\gamma) < 4 \times 10^{-5}$), \blacksquare ($4 \times 10^{-5} \leq Br(\tau \rightarrow \mu\gamma\gamma) < 5.8 \times 10^{-4}$), \bullet ($Br(\tau \rightarrow \mu\gamma\gamma) \geq 5.8 \times 10^{-4}$) to denote the results in different parameter spaces in the process $\tau \rightarrow \mu\gamma\gamma$.

Analysis of the relationship between $\tan\beta$ and $M_{\tilde{L}12}^2$ is shown in Fig.6(a). We are able to clearly find that \blacklozenge is mainly concentrated in the upper right corner. Then \blacktriangle , \blacksquare step by step, and \bullet is beyond the experimental limits ($Br(\tau \rightarrow \mu\gamma\gamma) \geq 5.8 \times 10^{-4}$), and they are mainly concentrated in the range of $5 < \tan\beta < 14$. In Fig.6(b) we plot the relationship between $\tan\beta$ and T_{e12} scattered points and find that each color is arranged like a triangle and is symmetric about $T_{e12} = 0$. The \blacklozenge is concentrated in $14 < \tan\beta \leq 50$. \blacktriangle is next to the blue color mainly in $7 < \tan\beta \leq 50$, followed by \blacksquare mainly in $8 < \tan\beta \leq 30$. The last \bullet beyond the experimental limit is mainly present in $6 < \tan\beta \leq 16$.

C. $\tau \rightarrow e\gamma\gamma$

Using the parameters $M_E^2 = 8 \times 10^5 \text{ GeV}^2$, $M_{\tilde{\nu}ij}^2 = 0$ ($i, j = 1, 2, 3, i \neq j$), $g_{YX} = 0.1$ we plot the diagrams of $Br(\tau \rightarrow e\gamma\gamma)$ affected by different parameters, and the same set of parameters is used to explore $Br(\tau \rightarrow e\gamma)$ and find the connection between them.

We study the effects of the parameters $M_{\tilde{E}13}^2$, T_{e13} , $M_{\tilde{L}13}^2$, g_X , $\tan\beta$, M_1 , μ and $M_{\tilde{L}}^2$ on $Br(\tau \rightarrow e\gamma\gamma)$ in Fig.7. In Fig.7(a)(e), we plot the relationship between $Br(\tau \rightarrow e\gamma\gamma)$,

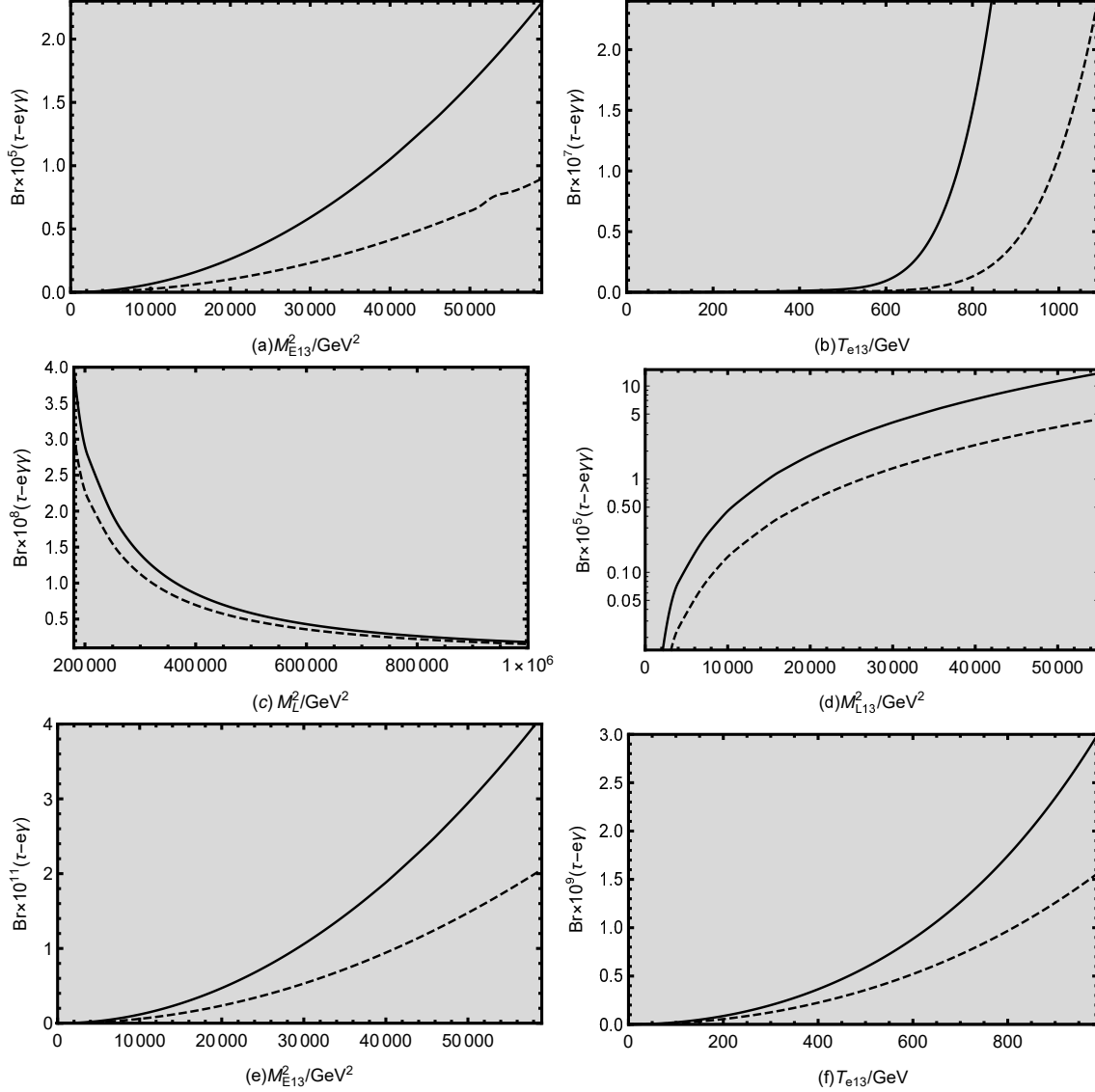


FIG. 7: $\text{Br}(\tau \rightarrow e\gamma\gamma)$ and $\text{Br}(\tau \rightarrow e\gamma)$ schematic diagrams affected by different parameters. The gray areas are reasonable value range, where $\text{Br}(\tau \rightarrow e\gamma\gamma)$ and $\text{Br}(\tau \rightarrow e\gamma)$ are lower than the upper limit. The dashed and solid lines in Fig.7(a)(e) correspond to $g_X = 0.4$ and $g_X = 0.3$. The dashed and solid lines in Fig.7(b)(f) $\tan\beta = 25$ and $\tan\beta = 20$. The dashed and solid lines in Fig.7(c) correspond to $M_1 = 1400$ GeV and $M_1 = 1000$ GeV. In Fig.7(d), with $\tan\beta = 15$, the dashed line corresponds to $\mu = 1300$ GeV and the solid line corresponds to $\mu = 1000$ GeV.

$\text{Br}(\tau \rightarrow e\gamma)$ and M_{E13}^2 , where the dashed lines correspond to $g_X = 0.4$ and the solid lines correspond to $g_X = 0.3$. The solid curve is larger than the dashed curve, and two lines increase with the increasing M_{E13}^2 . The solid and dashed lines are located in the gray area. In Fig.7(b)(f), the relationship between $\text{Br}(\tau \rightarrow e\gamma\gamma)$, $\text{Br}(\tau \rightarrow e\gamma)$ and T_{e13} are shown, and

the results are plotted with the dashed lines ($\tan \beta = 25$) and the solid lines ($\tan \beta = 20$), respectively. In Fig.7(b), we find very small values for the solid line at $0 < T_{e13} < 500$ GeV and for the dashed line at $0 < T_{e13} < 600$ GeV, but then increase substantially. In Fig.7(c), let $M_{\tilde{L}ij}^2 = 200$ GeV² ($i, j = 1, 2, 3, i \neq j$), with $M_1 = 1400$ GeV and $M_1 = 1000$ GeV corresponding to the dashed and solid lines, respectively, $\text{Br}(\tau \rightarrow e\gamma\gamma)$ varies with $M_{\tilde{L}}^2$. It can be clearly seen that both the solid and dashed lines show a decreasing trend. Let $g_X = 0.3$, $\tan \beta = 20$, $M_1 = 1000$ GeV, in Fig.7(d), we plot $\text{Br}(\tau \rightarrow e\gamma\gamma)$ versus $M_{\tilde{L}13}^2$. The dashed and solid lines indicate $\mu = 1300$ GeV, $\mu = 1000$ GeV, respectively. It is clear that $\text{Br}(\tau \rightarrow e\gamma\gamma)$ becomes larger as $M_{\tilde{L}13}^2$ increases and smaller as μ increases. In summary the parameters $M_{\tilde{E}13}^2$, T_{e13} , $M_{\tilde{L}13}^2$, μ , M_1 , g_X , $\tan \beta$ and $M_{\tilde{L}}^2$ have some influence on $\text{Br}(\tau \rightarrow e\gamma\gamma)$ and are the sensitive parameters.

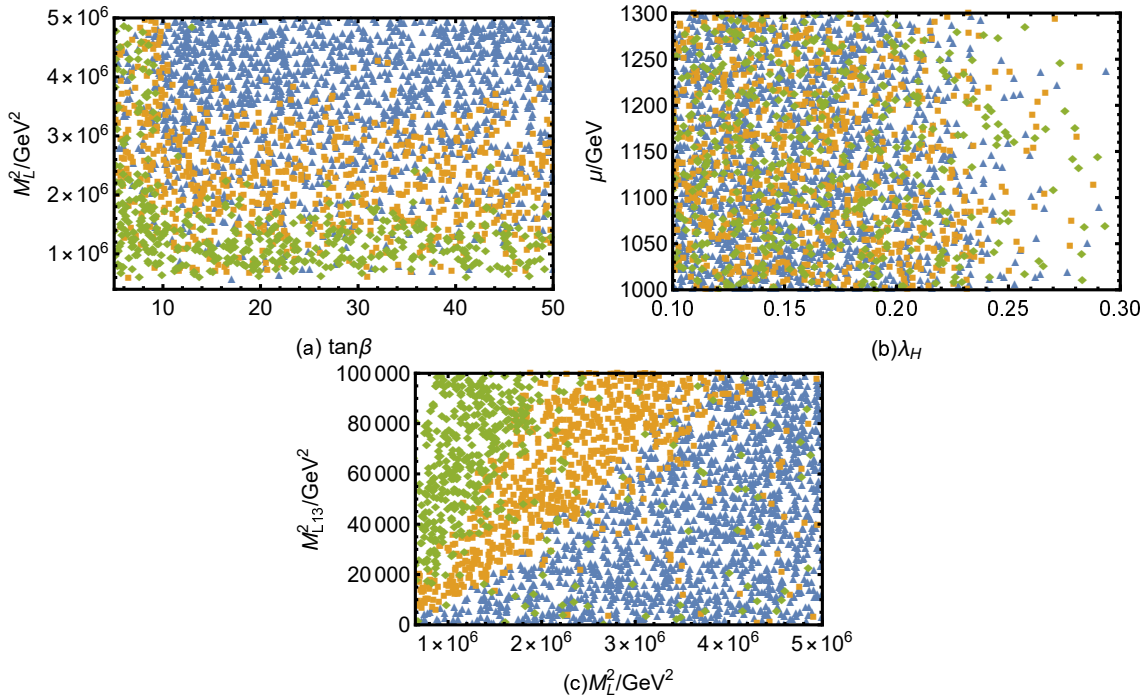


FIG. 8: Under the premise of current limit on LFV decay $\tau \rightarrow e\gamma\gamma$, reasonable parameter space is selected to scatter points, with the notation \blacktriangle ($0 < \text{Br}(\tau \rightarrow e\gamma\gamma) < 2 \times 10^{-6}$), \blacksquare ($2 \times 10^{-6} \leq \text{Br}(\tau \rightarrow e\gamma\gamma) < 2 \times 10^{-5}$), \blacklozenge ($2 \times 10^{-5} \leq \text{Br}(\tau \rightarrow e\gamma\gamma) < 2.5 \times 10^{-4}$).

Next, we randomly scan some parameters, namely those shown in Table II and Table V, according to which we obtain Fig.8. We use \blacktriangle ($0 < \text{Br}(\tau \rightarrow e\gamma\gamma) < 2 \times 10^{-6}$), \blacksquare ($2 \times 10^{-6} \leq \text{Br}(\tau \rightarrow e\gamma\gamma) < 2 \times 10^{-5}$), \blacklozenge ($2 \times 10^{-5} \leq \text{Br}(\tau \rightarrow e\gamma\gamma) < 2.5 \times 10^{-4}$) to denote the results in different parameter spaces in the process $\tau \rightarrow e\gamma\gamma$.

TABLE V: Scanning parameters for Fig.8

Parameters	M_{L13}^2 / GeV^2	T_{e13} / GeV	$T_{\bar{\nu}13} / \text{GeV}$
Min	0	- 400	- 400
Max	10^5	400	400

In Fig.8(a) we analyze the relationship between $\tan\beta$ and $M_{\tilde{L}}^2$. We are able to clearly find \blacktriangle is mainly concentrated in the upper right position, \blacksquare is mainly concentrated in the middle position, and \blacklozenge is mainly concentrated in the bottom. The value of the branching ratio shows an increasing trend from the upper right to the lower left. In Fig.8(b) we analyze the relationship between λ_H and μ . The points are very dense in the range of $0.1 < \lambda_H \leq 0.2$ and start to become sparse after $\lambda_H > 0.2$. In Fig.8(c) we analyze the relationship between $M_{\tilde{L}}^2$ and M_{L13}^2 . We find that the \blacklozenge is mainly concentrated in $4 \times 10^5 \text{ GeV}^2 < M_{\tilde{L}}^2 < 1.8 \times 10^6 \text{ GeV}^2$ (view from the above axis) and $2 \times 10^4 \text{ GeV}^2 < M_{L13}^2 < 1 \times 10^5 \text{ GeV}^2$ (view from the left axis), \blacksquare is mainly concentrated in $5000 \text{ GeV}^2 < M_{\tilde{L}}^2 < 3.8 \times 10^6 \text{ GeV}^2$ (view from the above axis) and $0 < M_{L13}^2 < 1 \times 10^5 \text{ GeV}^2$ (view from the left axis), \blacktriangle is mainly concentrated in $4 \times 10^5 \text{ GeV}^2 < M_{\tilde{L}}^2 < 3.8 \times 10^6 \text{ GeV}^2$ (view from the above axis) and $0 < M_{L13}^2 < 1 \times 10^5 \text{ GeV}^2$.

V. CONCLUSION

From the order of magnitude of branching ratios and data analysis, we know that the $\mu \rightarrow e\gamma$ process is more restrictive to LFV, based on which we investigate the LFV process of $l_j \rightarrow l_i\gamma\gamma$ in this paper. We have made use of the $U(1)_X\text{SSM}$, which has contribute to our study. We consider the Feynman diagrams of $l_j \rightarrow l_i\gamma\gamma$ and perform extensive calculations to draw line diagrams of the different parameters versus $\text{Br}(l_j \rightarrow l_i\gamma\gamma)$, followed by a large scan of the parameters. Numerical results show that $\text{Br}(\mu \rightarrow e\gamma\gamma)$, $\text{Br}(\tau \rightarrow \mu\gamma\gamma)$ and $\text{Br}(\tau \rightarrow e\gamma\gamma)$ are related to the leptonic flavor mixing parameters. By analyzing the values, we learn that the branching ratios can reach 10^{-12} for $\mu \rightarrow e\gamma\gamma$, 10^{-4} for $\tau \rightarrow \mu\gamma\gamma$, and 10^{-5} for $\tau \rightarrow e\gamma\gamma$. The branching ratios of the three processes in $U(1)_X\text{SSM}$ are very close to or even exceed their respective experimental upper limits. This provides a reference for other future work on leptonic flavor destruction.

We consider the constraints on the LFV branching ratio for $l_j \rightarrow l_i\gamma\gamma$. In the numerical

calculation, we include many parameters as variables, including $\tan\beta$, g_X , g_{YX} , λ_H , λ_C , μ , M_2 , $M_{\tilde{L}}^2$, $M_{\tilde{\nu}}^2$, $M_{\tilde{L}ij}^2$, $T_{\nu ij}$ and T_{eij} . By analyzing the numerical results, we find that a part of parameters have a great influence on the results. $M_{\tilde{L}}^2$, $M_{\tilde{E}}^2$, g_X , g_{YX} , M_2 and $\tan\beta$ are important parameters. $M_{\tilde{L}ij}^2$, T_{eij} , $M_{\tilde{E}ij}^2$, $M_{\tilde{\nu}ij}^2$ and $T_{\nu ij}$ are sensitive parameters. We also make comparison with certain parameters of the $l_j \rightarrow l_i\gamma$ processes and obtain that our work can satisfy the restrictions, which is very meaningful. To save space in the paper, we only compare and explain some parameters of the $l_j \rightarrow l_i\gamma$ processes. However, through comprehensive research, we prove that all parameters in our work satisfy the limitations of the $l_j \rightarrow l_i\gamma$ processes. In summary, we find that many parameters have a greater or lesser effect on LFV, but the non-diagonal elements corresponding to the initial and final leptons generation are the most sensitive to LFV. So we believe that the main sensitive parameters and sources leading to LFV are the non-diagonal elements involving the initial and final leptons. This work can benefit the detection of new physics.

Acknowledgments

This work is supported by National Natural Science Foundation of China (NNSFC)(No.12075074), Natural Science Foundation of Hebei Province(A2020201002, A2023201040, A202201022, A2022201017, A2023201041), Natural Science Foundation of Hebei Education Department (QN2022173), Post-graduate's Innovation Fund Project of Hebei University (HBU2023SS043, HBU2024SS042), the youth top-notch talent support program of the Hebei Province.

-
- [1] S. T. Petcov, Sov. J. Nucl. Phys. **25**, 340 (1977). JINR-E2-10176.
 - [2] K. Abe, et al. (T2K Collaboration), Phys. Rev. Lett. **107** (2011) 041801.
 - [3] J. Ahn, et al. (RENO Collaboration), Phys. Rev. Lett. **108** (2012) 191802.
 - [4] F. An, et al. (DAYABAY Collaboration), Phys. Rev. Lett. **108** (2012) 171803.
 - [5] L. Calibbi, G. Signorelli, Riv. Nuovo Cim. **41** (2018) 71.
 - [6] U. Ellwanger, C. Hugonie, A.M. Teixeira, Phys. Rep. **496** (2010) 1-77.
 - [7] B. Yan, S.M. Zhao, T.F. Feng, Nucl. Phys. B **975** (2022) 115671.

- [8] F. Staub, arXiv: 0806.0538.
- [9] F. Staub, Comput. Phys. Commun. **185** (2014) 1773.
- [10] F. Staub, Adv. High Energy Phys. **2015** (2015) 840780.
- [11] J. Rosiek, Phys. Rev. D **41** (1990) 3464.
- [12] Particle Data Group, Prog. Theor. Exp. Phys. (2022) 083C01.
- [13] F. Fortuna, et al., Phys. Rev. D **107** (2023) 1, 015027.
- [14] J. I. Aranda, et al. Phys. Rev. D **78** (2008) 017302.
- [15] T. T. Wang, S.M. Zhao, J.F. Zhang, et al., Eur. Phys. J. C **82** (2022) 7.
- [16] T. T. Wang, S.M. Zhao, X.X. Dong, et al., JHEP **04** (2022) 122.
- [17] B. Yan, S.M. Zhao, T.F. Feng, Nucl. Phys. B **975** (2022) 115671.
- [18] S. M. Zhao, L.H. Su, X.X. Dong, et al., JHEP **03** (2022) 101.
- [19] S. M. Zhao, T.F. Feng, M.J. Zhang, et al., JHEP **02**(2020) 130.
- [20] L. H. Su, S.M. Zhao, X.X. Dong, et al., Eur. Phys. J. C **81** (2021) 433.
- [21] S. M. Zhao, G.Z.Ning, J.J. Feng, et al., Nucl. Phys. B **969** (2021) 115469.
- [22] CMS collaboration, Phys. Lett. B **716** (2012) 30.
- [23] ATLAS collaboration, Phys. Lett. B **716** (2012) 1.
- [24] P. Cox, C.C. Han, T.T. Yanagida, Phys. Rev. D **104** (2021) 075035.
- [25] M. V. Beekveld, W. Beenakker, M. Schutten, et al., SciPost Phys. **11** (2021) 3, 049 [arXiv: 2104.03245].
- [26] M. Chakraborti, L. Roszkowski, S. Trojanowski, JHEP **05**(2021) 252 [arXiv: 2104.04458].
- [27] F. Wang, L. Wu, Y. Xiao, et al., Nucl. Phys. B **970** (2021) 115486 [arXiv: 2104.03262].
- [28] M. Chakraborti, S. Heinemeyer, I. Saha, Eur. Phys. J. C **81**(2021) 12, 1114 [arXiv: 2104.03287].
- [29] M. Endo, K. Hamaguchi, S. Iwamoto, et al., JHEP **07** (2021) 075 [arXiv: 2104.03217].